Wire Arc Additive Manufacturing of 308L Stainless Steel: Dimensional Characterization, Arc Stability, Microstructural Evolution, and Mechanical Anisotropy in Thin-Wall Structures

Manufactura aditiva de acero inoxidable 308L mediante arco y alambre: caracterización dimensional, estabilidad del arco, evolución microestructural y anisotropía mecánica estructuras de paredes delgadas

Theylor A. Amaya-Villabón [12], Andres F. Gil-Plazas [12], Oscar F. Mayorga-Rodríguez [1], Cristian R. Peña-Velandia [1], Julián D. Rubiano-Buitrago [23], David A. Ramírez-Vargas [4] and Liz K. Herrera-Quintero [2]

ABSTRACT

In this work, 308L stainless steel was deposited via wire arc additive manufacturing, identifying how process variables (voltage, wire feed speed, and travel speed) influence the geometry of the deposit in terms of arc stability, the resulting microstructure, and mechanical properties. Deposits were obtained by varying the voltage from 16 to 20V, the wire feed speed between 4 and 6 m/min, and the travel speed between 240 and 540 mm/min, in order to assess their importance in deposit quality and in the occurrence of defects such as porosity and inclusions. By varying the aforementioned parameters, the response values of the deposit (height and width) were obtained, which is crucial for understanding and controlling the material deposition layer by layer, as well as for properly planning process trajectories. Proper control of welding conditions allows for uniform layers with lower porosity, better internal quality, and an austenitic matrix microstructure with delta ferrite, whose morphology varies with heat input. Finally, through the effective control of height and width, we obtained a thin wall was obtained to evaluate its mechanical behavior. The results demonstrated proper interlayer adhesion as well as anisotropy, particularly regarding tensile strength and ductility, depending on the orientation of the specimens relative to the deposition direction.

Keywords: wire arc additive manufacturing, 308L stainless steel, dimensional characterization, arc stability, microstructural behavior, mechanical anisotropy

RESUMEN

En este trabajo, se depositó acero inoxidable 308L mediante fabricación aditiva por arco con hilo, identificando cómo las variables del proceso (voltaje, velocidad de alimentación del alambre y velocidad de avance) influyen en la geometría del depósito en términos de estabilidad del arco, microestructura resultante y propiedades mecánicas. Los depósitos se obtuvieron variando el voltaje entre 16 y 20 V, la velocidad de alimentación del alambre entre 4 y 6 m/min y la velocidad de avance entre 240 y 540 mm/min, con el fin de evaluar su importancia en la calidad del depósito y en la aparición de defectos como porosidad e inclusiones. Al variar los parámetros mencionados, se obtuvieron los valores de respuesta del depósito (altura y ancho), lo cual es fundamental para comprender y controlar la deposición del material capa por capa, así como para planificar adecuadamente las trayectorias del proceso. Un control adecuado de las condiciones de soldadura permite obtener capas uniformes con menor porosidad, mejor calidad interna y una microestructura de matriz austenítica con ferrita delta, cuya morfología varía con el aporte térmico. Finalmente, mediante el control efectivo de la altura y el ancho, se obtuvo una pared delgada para evaluar su comportamiento mecánico. Los resultados demostraron una adecuada adhesión entre capas, así como anisotropía, particularmente en cuanto a la resistencia a la tracción y la ductilidad, dependiendo de la orientación de las probetas con respecto a la dirección de deposición.

Palabras clave: manufactura aditiva mediante arco y alambre, acero inoxidable 308L, caracterización dimensional, estabilidad del arco, comportamiento microestructural, anisotropía mecánica

1 SENA Regional Distrito Capital – Centro de Materiales y Ensayos. Correspondence: agilp@sena.edu.co

2 Universidad Nacional de Colombia, Facultad de Ingeniería.

3 Universidad de los Llanos – Facultad de Ciencias Básicas e Ingenierías.

4 Linde PLC, Colombia.

Introduction

Additive manufacturing (AM), commonly referred to as *3D printing*, is a process in which components are built layer by layer from a digital 3D model [1]. In recent years, AM has become increasingly attractive to various industries due to its potential for reducing material consumption, minimizing environmental impact, and enabling the manufacturing of complex geometries that are challenging or impossible to achieve through conventional processes [2-3].

According to ISO/ASTM 52900:2021 [4], AM technologies can be classified into seven categories, out of which three are predominantly used in metallic systems: powder bed fusion (PBF), directed energy deposition (DED), and binder jetting (BJ). In PBF processes, such as laser powder bed fusion (LPBF), also referred to as *selective laser melting* (SLM), a focused heat source (laser or electron beam) selectively melts regions of a powder bed to consolidate the material [5-6]. In contrast, DED processes, including laser metal deposition (LMD), wire laser additive manufacturing (WLAM), and wire arc additive manufacturing (WAAM), employ a focused energy source to melt metallic feedstock (either powder or wire) as it is deposited [7-8]. Meanwhile, BJ involves selectively depositing a liquid binding agent onto a powder bed, with final densification commonly achieved through a shaping-debinding-sintering (SDS) route [9–10].

This accurate distinction between PBF, DED, and BJ is essential, as each category has unique process mechanisms, feedstock requirements, and potential applications, which dictate its suitability for different industrial sectors.

Among the DED processes, wire-based methods such as WLAM and WAAM offer the advantage of significantly higher deposition rates compared to PBF or SDS-based routes [11-12]. However, these processes often result in a limited surface quality, which usually requires machining, necessitating hybrid manufacturing strategies [13-14].

Despite its potential, WAAM remains relatively unexplored in Colombia, particularly regarding the study of solidification phenomena and their impact on mechanical properties and microstructural evolution [15-17]. Given WAAM's strong connection to welding processes, its adoption in the Colombian metalworking industry is feasible due to the existing expertise in this field [18]. WAAM traces its origins back to Baker's 1920 patent, which introduced the concept of *moving electrodes* for layer-by-layer deposition. Today, this concept has evolved into a controlled process where a filler wire is melted using an electric arc and guided through numerical control systems [19].

Common austenitic stainless steels (*e.g.*, 304 and 308) are widely used due to their excellent corrosion resistance and mechanical properties [20]. With a composition of approximately 18% chromium and 8% nickel, 304 offers outstanding durability, making it ideal for applications in the food, chemical, and medical industries. Meanwhile, 308 is a preferred filler material for welding 304, ensuring strong and reliable joints [21]. The versatility and resilience of these stainless steels make them essential in environments where durability and resistance to harsh conditions are critical [14].

While WAAM has been extensively studied in terms of process optimization and material properties, there is a lack of comprehensive studies that analyze the precise effects of process variables such as voltage, wire feed speed, and travel speed on layer uniformity, microstructural evolution, and mechanical behavior in 308L stainless steel. Previous research has focused on deposition rates and overall mechanical properties, but there is still a need a deeper understanding of how these variables influence defect formation (*e.g.*, porosity, inclusions) and anisotropic behavior in printed components.

This study hypothesizes that, by carefully controlling WAAM process parameters, it is possible to improve layer uniformity, reduce defects, and enhance mechanical performance in 308L stainless steel components. Specifically, optimizing voltage, wire feed speed, and travel speed may lead to better control over the deposit geometry, resulting in high-quality, structurally sound components.

Materials and methods

The overall methodological workflow for exploring the WAAM process applied to 308L stainless steel is illustrated in Fig. 1.

Raw materials

In this study, a 308L stainless steel wire with a diameter of 0.035 in was used, whose chemical composition is listed in Table I. We employed a protective gas composed of 95% Ar, 3% CO_2, and 3% N_2 (Linde PLC) during gas metal arc welding (GMAW), with a flow of 35 CFH.

Table I. Chemical composition of 308L stainless steel

Element	Weight %
C	0.036
Si	0.516
Mn	1.746
Cr	19.67
Ni	10.78
Mo	0.113
P	0.025
S	0.014

WAAM equipment

The WAAM setup employed in this study integrated a GMAW power source, a three-axis computer numerical control (CNC) router, dedicated control software, and a series of

custom software tools for controlling the welding torch and a forced-convection fan between passes.

GMAW power source and deposition setup

A SKY MIG 4060 TX (SWEISS) GMAW unit served as the primary deposition source. The machine was configured for short-circuit transfer under constant voltage conditions. The previously specified filler metal and shielding gas were delivered through a standard GMAW torch mounted on the CNC router's Z-axis head assembly. This arrangement ensured adequate weld pool protection and minimized atmospheric contamination during deposition.

CNC router integration and control

As the mechanical platform, a DW1010 CNC router (DWIN) originally designed for subtractive manufacturing was adapted for WAAM. The system's three-axis motion stage (X, Y, Z) provided accurate deposition paths. The router's spindle control signals were repurposed to manage peripheral WAAM components. Instead of controlling a cutting spindle, these signals were rerouted through a dual-output relay module that switched critical deposition peripherals on or off, *i.e.*, the welding torch arc initiation and an auxiliary cooling fan. This reconfiguration enabled fine-grained on/off control of the deposition arc and ancillary devices using spindle speed commands from the CNC control interface.

The CNC system was controlled using NCStudio software, which interpreted G-code commands to orchestrate stepper motor movements and trigger digital I/O lines. Limit switches on all axes were retained for positional references and safety limits. Pulse and direction signals (X PULSE, X DIR, Y PULSE, Y DIR, Z PULSE, Z DIR) ensured precise axis motion, while the adapted spindle commands (SPFFD) managed the WAAM peripherals (Fig 2.).

Toolpath generation and post-processing

Toolpaths were generated using UltiMaker Cura, which, although primarily designed for thermoplastic extrusion, was selected for its flexibility in slicing and producing G-code toolpaths. These toolpaths served as the primary means of communication between the control and welding machines [22-24]. The build volume and nozzle diameter were set in Cura to simulate a custom FFF printer with a large format working envelope. Layer heights, line widths, and print speeds in Cura's slicing settings were tuned to reflect arc and wire deposition characteristics rather than polymer extrusion.
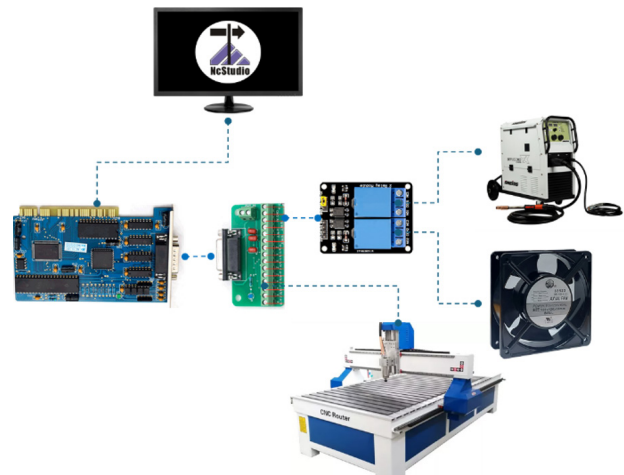

Figure 2. Integrated WAAM system with NCStudio control, the GMAW source, and peripheral activation relays
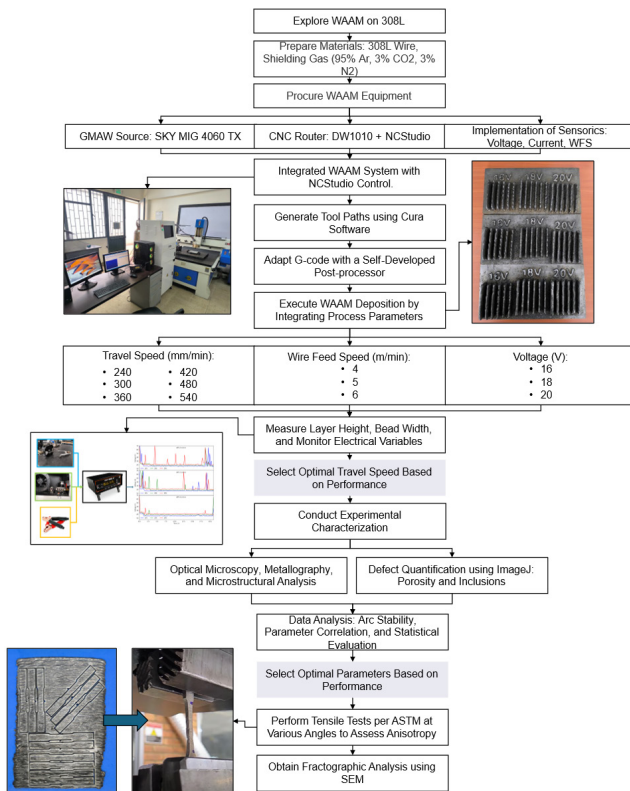**Source:** Authors

Figure 1. Methodological workflow for the exploration of the WAAM process applied to 308L stainless steel
Source: Authors

However, the Cura-generated G-code required further customization in order to be compatible with NCStudio and incorporate welding-specific commands. A custom Python-based postprocessor was developed to translate Cura's spindle speed commands into relay activation signals, to insert dwell times for thermal stabilization between layers, and to manage arc initiation delays. This postprocessor introduced waiting periods, pre- and post-travel delays, and tool maintenance positions, each serving a distinct yet essential role. Pre-travel delays ensured that the arc had sufficient time to stabilize before initiating movement, thereby preventing inadequate material deposition and preserving layer integrity at the start of the weld bead. Meanwhile, dwell times were used between passes to allow the deposited material to cool, reducing excessive thermal buildup and mitigating defects associated with overheated

layers. Without these deliberate pauses, immediate motion upon arc ignition would compromise the initial bead quality, and insufficient cooling intervals would increase the likelihood of thermally induced defects, adversely affecting the overall build quality. The postprocessor's interface and the parameter values employed are presented in Fig. 3.

Monitoring and data acquisition systems

A weld data logger (CWT WDL-3) was integrated for continuously recording operational variables such as arc voltage, current, and wire feed speed during the deposition process. Communication with the data logger was established via the RS232 serial interface and handled using Python scripts. The acquired time-stamped data were later used to validate process stability, correlate input parameters with the resulting bead geometry, and guide process optimization.
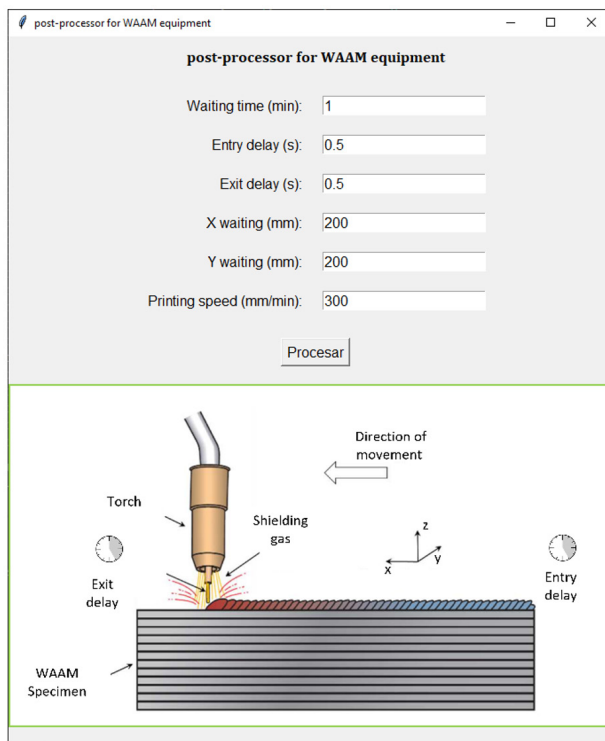

Figure 3. Post-processor interface
Source: Authors

Characterization

Additive deposit dimensions (height and width) were measured with a Vernier caliper (Mitutoyo), and electrical variables were monitored using the CWT WDL-3 (Lincoln Electric). Microstructural evolution was assessed via stereo microscopy (Zeiss Axio Observer V8), metallography (Zeiss Axio Observer Z1.m) following ASTM E3 guidelines, and scanning electron microscopy (SEM) coupled with energy-dispersive X-ray spectroscopy (EDS) (Phenom XL). The percentage of inclusions and porosity was quantified using the ImageJ software and grayscale thresholding. Finally,

mechanical properties were evaluated via tensile testing (SHIMADZU UH-50A) in accordance with ASTM E8/E8M.

Results analysis and discussion

Parametric influence on WAAM deposition geometry

Initially, an exploratory parameter matrix was implemented to examine the combined influence of voltage (16, 18, and 20 V), wire feed speed (4, 5, and 6 m/min), and travel speed (240-540 mm/min) on bead geometry. Ten layers were deposited under each set of conditions, and both width and height were measured to assess deposition behavior. The purpose of this preliminary stage was to identify the boundaries of a stable process window that was suitable for subsequent quantitative analysis.

Figs. 4 and 5 present the experimental matrix from the top and lateral perspectives, respectively, with voltage levels (20, 18, and 16 V) in the columns and wire feed speeds (6, 5, and 4 m/min) in the rows. In each matrix image, walls consisting of ten stacked beads were deposited, with each wall built at different travel speeds, i.e., 240, 300, 360, 420, 480, and 540 mm/min. These speeds increase from right to left in Fig. 4 (top view) and from bottom to top in Fig. 5 (side view). The yellow rectangles highlight the conditions under which pronounced humps and valleys appear, i.e., unstable depositions at higher travel speeds.

A visual inspection confirmed that, at all voltage levels, increasing travel speed progressively destabilized the deposition, producing macroscopic defects such as humps and valleys [25]. These irregularities are consistent with widely reported mechanisms in welding and WAAM literature, where an excessive travel speed promotes the backward flow of liquid metal, leading to the periodic accumulation of molten material along the bead [26]. Such hump formation has been explained using hydrodynamic models that consider the balance between backward liquid flow, capillary forces, and solidification dynamics [27]. Furthermore, the width and reinforcement of the deposited layer are strongly influenced by the interaction between travel speed, wire feed rate, and arc stability [28]. In this study, when the voltage-to-wire speed ratio was low, an insufficient molten material supply, in addition to arc instability, exacerbated these effects, resulting in incomplete fusion and pronounced surface irregularities.

While 20 V provided relatively stable beads across all wire feed speeds, lower voltages (18 and 16 V) and reduced wire feed speeds (4 to 5 m/min) exacerbated deposition irregularities due to the lower heat input and material supply. Based on these observations, travel speeds above 300 mm/min—where humps and valleys predominated across most voltages—were excluded from further analysis, as they were outside the feasible WAAM process window.
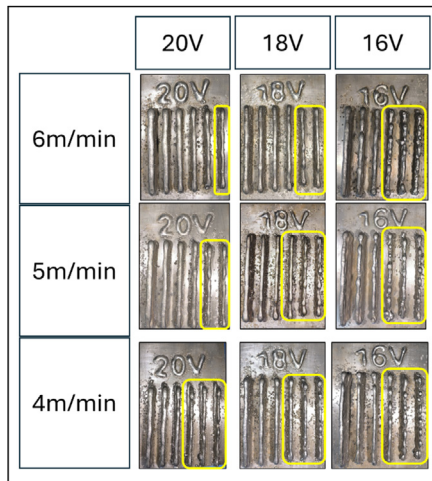
Figure 4. Top view of humps and valleys observed under different parameter combinations
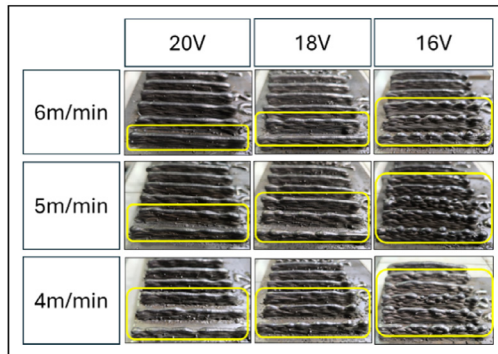**Source:** Authors

Figure 5. Lateral view of humps and valleys observed under different parameter combinations
Source: Authors

Hereafter, the discussion focuses on the stable deposition conditions observed at 240 and 300 mm/min, where dimensional control was achievable. The resulting average layer heights are shown in Fig. 6, while the corresponding bead widths are plotted in Fig. 7.
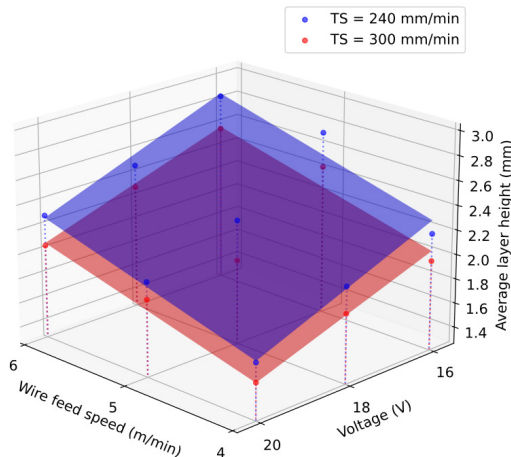

Figure 6. Average layer height *vs.* wire feed speed and voltage at TS = 240 mm/min (blue) and TS = 300 mm/min (red)
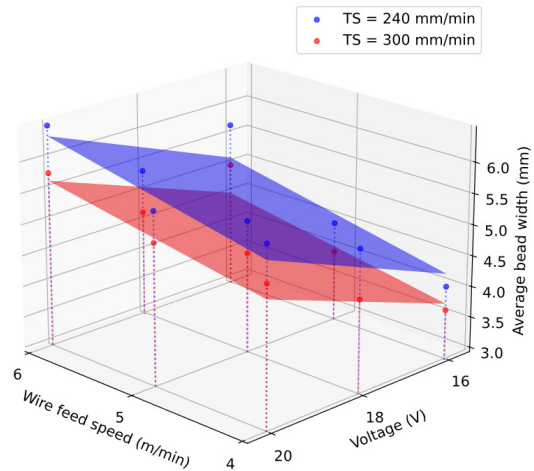**Source:** Authors.

Figure 7. Average bead width *vs.* wire feed speed and voltage at TS = 240 mm/min (blue) and TS = 300 mm/min (red)
Source: Authors

In Fig. 6, note that the layer height decreases as the voltage increases, while it rises with higher wire feed speeds (WFS). The increase in voltage introduces a greater heat input, leading to a more laterally spread bead at the expense of its vertical build-up. This is further evidenced in Fig. 6, where bead width becomes larger as voltage and WFS increase. At higher WFS, additional material is supplied, resulting in a greater deposited volume, thus broadening and elevating the bead. Conversely, higher travel speeds reduce the amount of deposited material per unit length, producing overall smaller dimensions in terms of both width and height. Notably, the data points lie close to their corresponding trend planes, indicating a nearly linear response of the geometric dimensions to changes in the input parameters within the tested ranges. This near-linearity suggests that, within these operational windows, it is possible to estimate and control the layer height and bead width of WAAM deposits by appropriately adjusting the voltage, WFS, and travel speed.

The behavior observed in our experiments is consistent with recent findings in the WAAM literature. For instance, [29] demonstrated that the control of variable layer heights in WAAM is highly dependent on a balanced interplay between heat input and material feed, where increases in voltage tend to produce wider, flatter beads. This aligns with our observation of reduced layer height and increased bead width at higher voltages. Similarly, using design of experiments (DOE) and analyses of variance (ANOVA), [30] reported that higher WFS significantly enhance material deposition, while higher travel speeds diminish the deposited volume, resulting in smaller bead dimensions. These studies validate our findings and underscore the critical role of parameter optimization in achieving stable and geometrically controlled WAAM deposits.

Electrical behavior

We acquired data on voltage, current, and actual WFS values at both 240 and 300 mm/min to assess arc stability under the

selected parameter sets. Fig. 8 presents the voltage profiles over time for a single deposited bead. Ideally, in a constant-voltage process, the measured voltage should remain close to the set point. However, we observed distinct voltage spikes well above the target value. These peaks indicate moments of arc instability, which disrupt the continuity of the deposition.

The results show that, at 300 mm/min, a greater number of voltage spikes occurred in comparison with 240 mm/min. This observation aligns with the previously noted macroscopic defects in the deposited material, as higher travel speeds exacerbate instability and yield more pronounced irregularities. Furthermore, at a given voltage, increasing the WFS contributed to more stable voltage readings. For instance, at 20 V and low WFS values, significant instability was apparent for both travel speeds. However, increasing the WFS to 6 m/min considerably improved voltage stability. At lower voltages (16 and 18 V), acceptable stability was achieved, with a WFS as low as 5 m/min. These findings suggest that higher voltages demand a greater filler material feed rate to maintain a stable arc, reinforcing the relationship between voltage, WFS, and the overall process stability.

To further evaluate the overall arc behavior, the heat input was calculated from the measured variables using Eq. (1)

$$Heat\ input = \frac{V * I}{TS} * 80\% \qquad (1)$$

Here, V is the voltage, I the current, and TS the travel speed. The factor 0.8 represents the thermal efficiency for a GMAW process, meaning that only about 80% of the electrical energy effectively contributes to weld pool formation.

By examining the coefficient of variation (CV) of the heat input for each deposited bead, it was possible to quantify the relative fluctuations in these parameters. A higher CV indicates greater variability in the monitored variables, and thus more instability in the process.

Fig. 9 illustrates the CV of the heat input as a function of the set voltage and WFS, which is represented using box-and-whisker plots. Each plot corresponds to a specific combination of voltage and WFS and includes data from multiple deposited beads (e.g., 10 beads per box, with each point representing one bead). Lower CV values signify more stable arc conditions.

At 18 and 20 V, increasing the WFS led to a reduction in the CV, confirming that higher WFS values aid in stabilizing the arc when operating at higher voltages. In contrast, at 16 V, the CV remained relatively constant regardless of the WFS, indicating that even the lowest WFS tested was already sufficient for maintaining a stable arc at this lower voltage level. These findings align with previous observations, emphasizing the importance of tuning the WFS to the

applied voltage in order to achieve stable WAAM deposition conditions.

Our findings are consistent with the work presented in [31], where a high-performance WAAM process for aluminum alloys was implemented using a controlled short-circuiting metal transfer approach. This study highlights that increased travel speeds can lead to higher instability in the arc, which aligns with the voltage spikes observed at 300 mm/min during our experiments. Furthermore, the results of the cited research indicate that balancing WFS with heat input is critical to maintaining arc stability, a key observation that also became evident in our study.

Similarly, [32] investigated the shaping of structural elements using WAAM, emphasizing the compensatory effect between current magnitude and travel speed on geometric parameters. Their study supports our conclusion that WFS plays a crucial role in stabilizing the arc, particularly at higher voltage levels. Moreover, they demonstrated that increased arc instability at excessive travel speeds leads to geometric inconsistencies in the deposited layers, further reinforcing our findings that travel speeds beyond 300 mm/min induce arc fluctuations and macroscopic defects. These validations provide a broader understanding of WAAM arc stability, emphasizing the significance of carefully optimizing voltage, travel speed, and WFS to minimize process variability.

Porosity and inclusions

To further evaluate the integrity of the deposited material under various parameter combinations, cross-sectional specimens were prepared and examined. The samples were cut perpendicular to the deposition direction and observed under a stereomicroscope at 100X magnification without etching, enabling the identification of defects such as non-metallic inclusion, porosity, and lack of fusion.
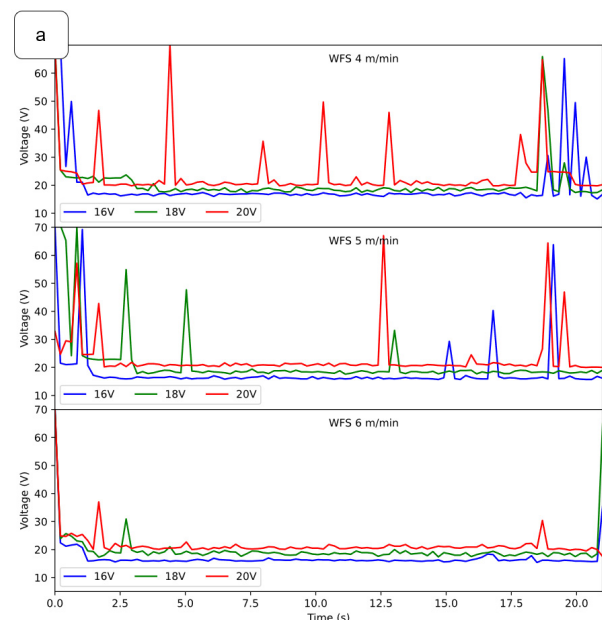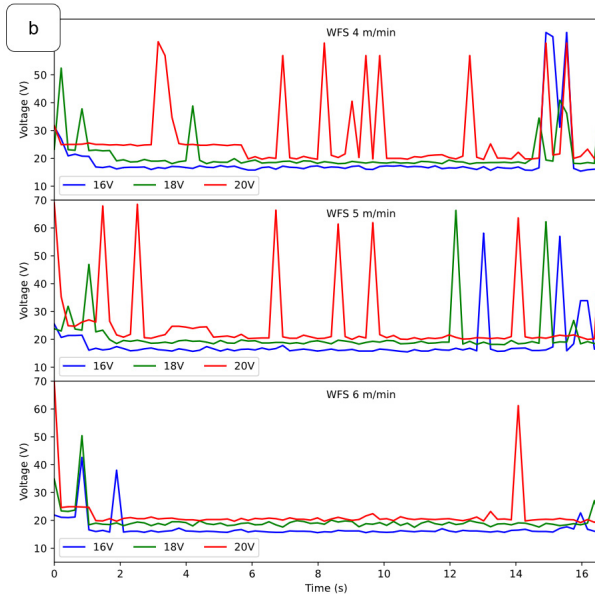
Figure 8. Voltage behavior over time under varying combinations of voltage, WFS, and travel speed. a) 240mm/min, b) 300mm/min.
Source: Authors

Fig. 10, presents two representative micrographs: one sample exhibiting a relatively high incidence of defects (20 V, TS=300 mm/min, WFS=4 m/min) and another showing a significantly lower defect count (20 V, TS=240 mm/min, WFS=6 m/min). When comparing these images, it becomes evident that certain parameter sets are more prone to inducing defects in the deposited structure.
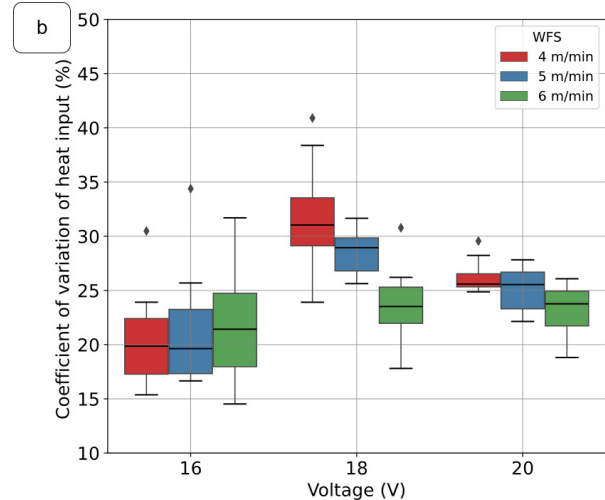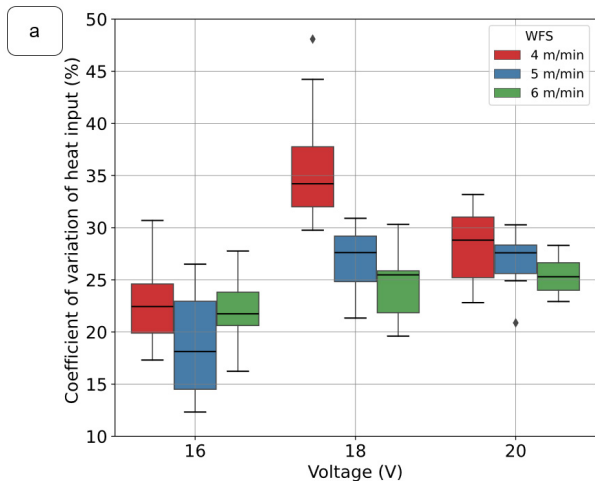

Figure 9. Coefficient of variation for the heat input under different combinations of voltage and WFS, reflecting arc stability across tested conditions. a) 240mm/min, b) 300mm/min.
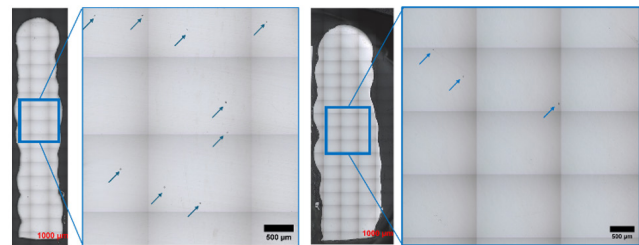**Source:** Authors

Figure 10. Micrographs showing defects (arrows indicate porosity and inclusions) for 20 V, TS = 300 mm/min, and WFS = 4 m/min (left); and 20 V, TS=240 mm/min, WFS=6 m/min (right)
Source: Authors

To quantify these discontinuities, a quantitative analysis of defect percentages was conducted in ImageJ. Grayscale thresholding methods were applied to binarize micrographs and measure the area fraction of defects. The resulting data, shown in Fig. 11 is plotted as a function of the (WFS), illustrating a clear trend, *i.e.*, lower WFS values correlated with higher defect percentages. This outcome aligns with the previously observed arc instabilities at lower WFS, underscoring the direct link between arc stability and defect formation. In other words, the parameter combinations that promoted arc instability also led to increased defect presence, emphasizing the importance of carefully tuning WFS, voltage, and travel speed to achieve both consistent geometric features and high-quality, defect-minimized WAAM deposits.

Recent findings in the WAAM literature align with these results. [31] demonstrated that optimizing the metal transfer mode significantly reduces porosity levels in WAAM processes. Their study on aluminum alloys showed that controlling short-circuiting metal transfer and adjusting wire feed speed effectively reduced defect rates, confirming that balancing deposition parameters is crucial for minimizing internal porosity. Similarly, [33] examined the impact of welding parameters on defect formation in

WAAM structures, finding that high energy input combined with low wire feed speeds led to increased porosity due to excessive heat retention and gas entrapment. These studies validate the findings and highlight the importance of parameter optimization in achieving defect-minimized WAAM components.
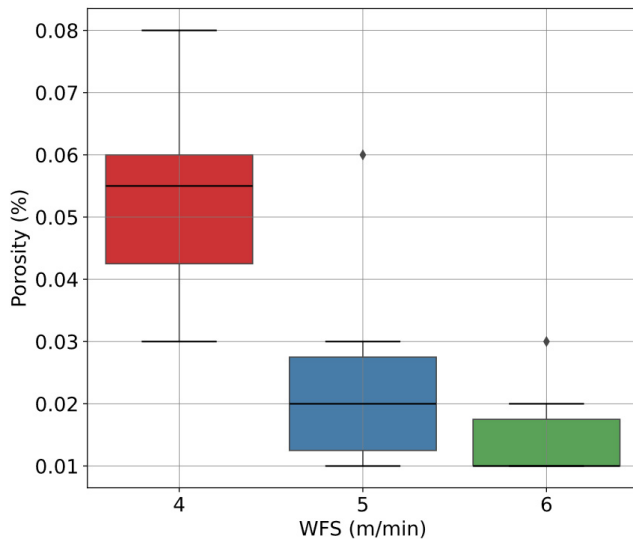

Figure 11. Percent porosity as a function of WFS
Source: Authors

Figure 12. Chemically etched WAAM-fabricated 308L stainless steel samples showing microstructural characteristics. (A) Columnar δ-ferrite near the fusion line, (B) transition from columnar to vermicular δ-ferrite, and (C) vermicular and lathy δ-ferrite morphologies in central and top regions of the layers.
Source: Authors

Microstructural analysis

With the objective of examining their microstructure, the WAAM specimens were chemically etched. Under all tested conditions, a similar microstructural behavior was observed, as shown in Fig. 12. The microstructure of WAAM-fabricated 308L stainless steel exhibited a complex interplay between the γ-austenite and δ-ferrite phases, along with minor inclusions, consistent with observations reported in the literature for similar materials and processes [34-36]. A repeating pattern was detected along the building direction, characterized by columnar dendrites in the bottom interface zone and a combination of vermicular and lathy ferrite morphologies in the central and top regions of each layer. This hierarchical structure stems from the thermal gradients inherent to the layer-by-layer deposition process.

The γ-austenite phase predominated across the cross-section, with δ-ferrite localized near fusion zones and along grain boundaries. The proportion and morphology of δ-ferrite were influenced by the heat input, transitioning from lathy to more vermicular forms as the heat input increased. This behavior can be attributed to slower cooling rates at higher heat inputs, which promote ferrite spheroidization and grain coarsening. These findings are aligned with those reported by [36], who observed similar transformations of ferrite morphologies under varying thermal conditions.
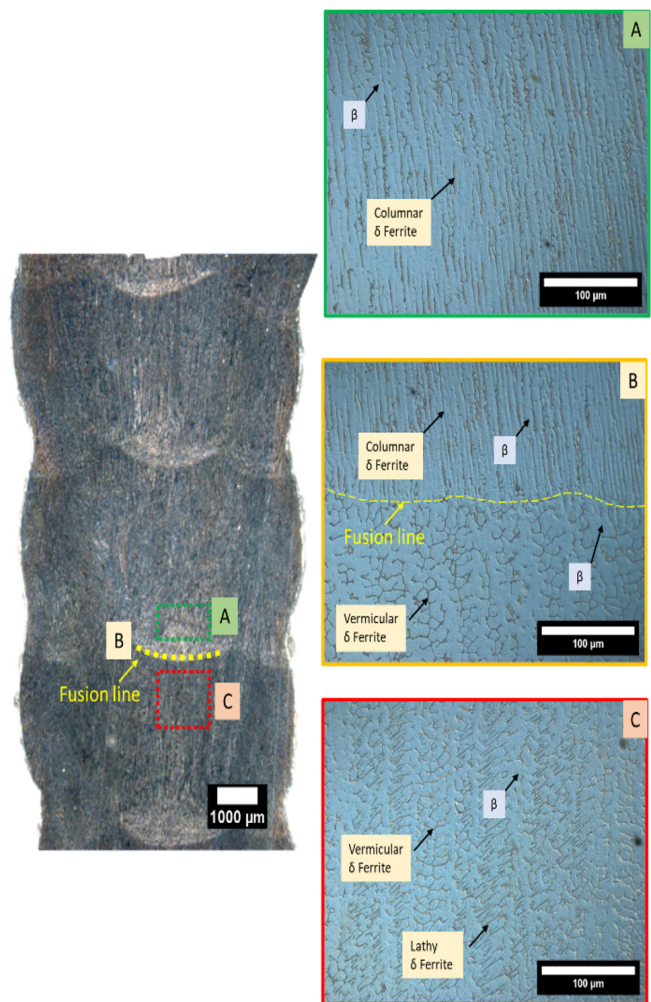
Mechanical properties and anisotropy

To evaluate the mechanical behavior of the WAAM-produced geometries, process parameters that demonstrated the best arc stability, the fewest non-metallic inclusions, and the widest single-bead profiles were selected. Using these conditions, a single-wall structure was constructed, with a width of one bead and a height of 100 layers (Fig. 13a). The tensile specimens were extracted using water jet cutting to ensure precision and mitigate the thermal effects that could alter the material's properties. The dimensions of the specimens were prepared in accordance with ASTM E8/E8M.

This configuration allowed for the extraction of tensile specimens oriented at 0, 45, and 90° relative to the travel direction of the CNC system (Fig. 13b). By testing samples from these different orientations, it was possible to assess the degree of anisotropy in the mechanical properties. Based on the previous analyses, the selected voltage, travel speed, and WFS values were 20 V, 240 mm/min, and 6 m/min.
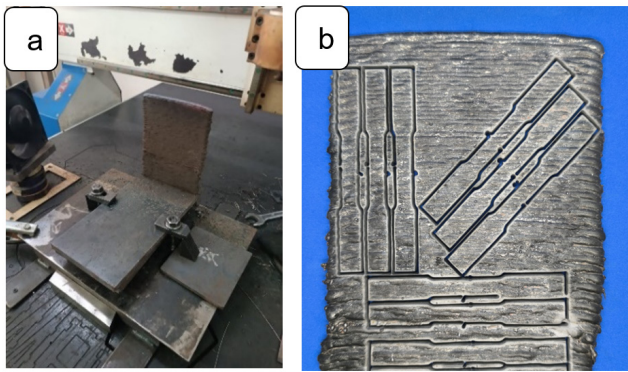
Figure 13. (a) WAAM-fabricated single-wall structure (100 layers) and (b) orientation layout of tensile specimens (0, 45, and 90˚) extracted via water jet cutting for anisotropy assessment.
Source: Authors

Fig. 14 presents the representative stress-displacement curves for three specimens tested at 0, 45, and 90˚ relative to the deposition direction. At first glance, the yield strengths appear similar across all three angles. This observation is confirmed by the yield strength data displayed in Fig. 15, where no discernible trend or angular influence is evident. An ANOVA performed on the yield strength results (Table II) further supports this conclusion, indicating that the testing angle does not exert a statistically significant effect on yield strength.
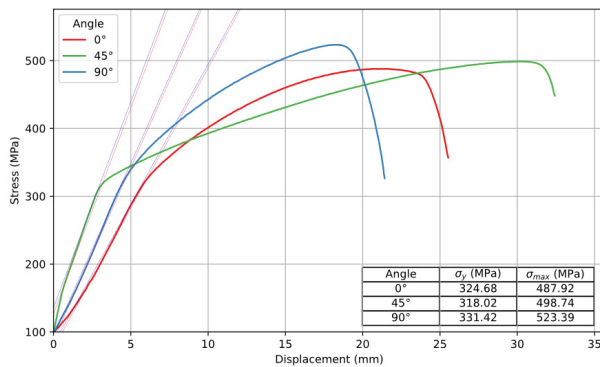

Figure 14. Stress-displacement curves for representative tensile specimens tested at 0, 45, and 90˚ relative to the deposition direction
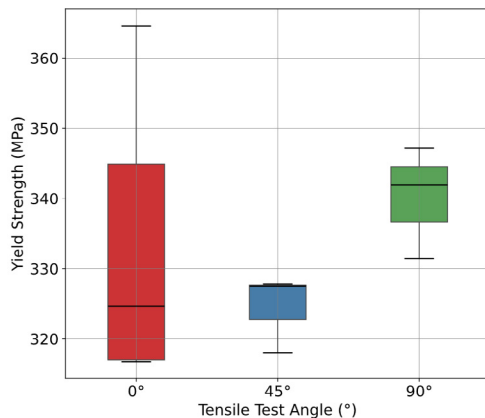**Source:** Authors

Figure 15. Box-and-whisker plot of the yield strength values for the specimens tested at 0, 45, and 90˚ relative to the deposition direction, showing no statistically significant influence of orientation on yield strength
Source: Authors

Table II. Results of the one-way ANOVA regarding yield strength

Source	Sum_sq	Df	F	*p*-value
Tensile test angle	376.627	2	0.78654	0.4877
Residual	1915.358	8		

Source: Authors

In contrast, the ultimate tensile strength (UTS) exhibits a clear dependence on orientation. As shown in Fig. 16, the UTS increases from an average of about 485 MPa at 0˚ to approximately 525 MPa at 90˚. This increase suggests that the bonding between the deposited layers is robust; the tensile force, which effectively acts to separate these layers, encounters greater resistance at 90˚. Such behavior can be attributed to directionally solidified, dendritic grain structures that enhance interlayer cohesion. The ANOVA for UTS (Table III) confirms this influence, yielding a *p*-value of 0.01 and establishing orientation as a statistically significant factor.
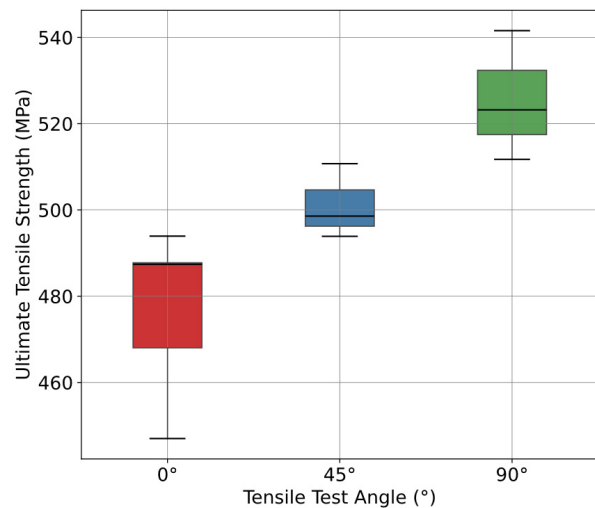

Figure 16. Box-and-whisker plot of UTS for specimens tested at 0, 45, and 90˚, highlighting a clear increase with orientation
Source: Authors

Table III. Results of the one-way ANOVA for UTS

Source	Sum_sq	Df	F	*p*-value
Tensile test Angle	4522.507	2	8,6313	0.010056
Residual	2095.86	8		

Source: Authors

A similar trend is observed in the elongation at fracture, which shows a pronounced increase at 45˚ in comparison with the other orientations. Both the stress-displacement curves and the grouped elongation data (Fig. 17) highlight this effect. The ANOVA for elongation (Table IV), with a *p*-value of 0.000195, indicates the statistically significant influence of orientation on ductility. This anisotropic behavior likely stems from preferential crystallographic

orientations that enable greater plastic deformation at certain angles. To further elucidate this phenomenon, future work should employ texture analysis techniques such as electron backscatter diffraction (EBSD), aiming to investigate the crystallographic orientation and its impact on mechanical behavior.
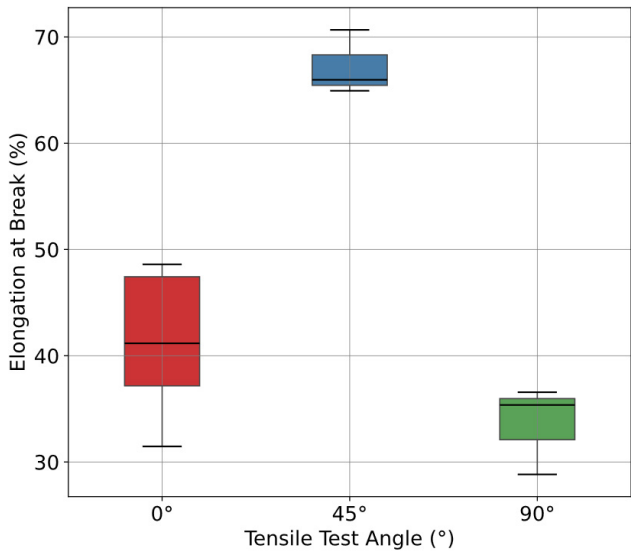

Figure 17. Box-and-whisker plot of elongation at fracture for specimens tested at 0, 45, and 90°, showing a significant increase in ductility at 45°
Source: Authors

Table IV. Results of the one-way ANOVA of Elongation at break.

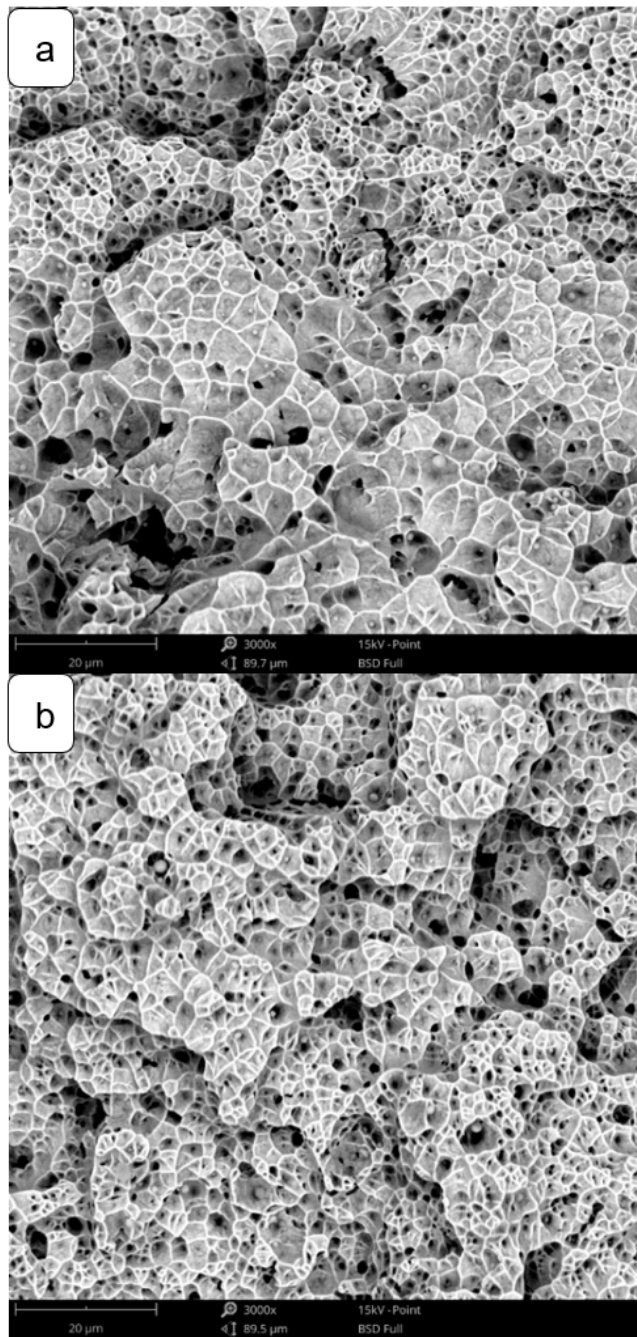| Source	Sum_sq	Df	F	p-value
Tensile test angle	1925.392	2	29.8585	0.000195
Residual	257.934	8		

Source: Authors

Fractographic analysis of tensile specimens

The fractures of the tensile specimens tested at 0, 45, and 90° were analyzed using SEM to examine the fracture surfaces in detail. Across all three orientations, a ductile fracture morphology was observed, characterized by a dimpled surface that was indicative of microvoid coalescence (Fig. 18). This is consistent with the typical behavior of ductile metals, where stress induces the formation and growth of microvoids that eventually coalesce to form dimples on the fracture surface.

At 90°, however, the fracture exhibited a noticeable directional pattern (Fig. 18c), aligning with the interlayer boundaries of the deposited structure. This directional fracture suggests that the dendritic grain growth observed in the microstructural analysis influenced the fracture path. The grain alignment, formed during the WAAM process due to directional solidification, likely guided the progression of the fracture, resulting in an anisotropic failure mode.

The tensile tests revealed the anisotropic behavior of the mechanical properties, particularly in the plastic region, which aligns with the microstructural characteristics produced by the WAAM process. The directional grain growth and interlayer boundaries observed in the microstructure directly influenced the mechanical response, particularly the UTS and the elongation at fracture. This anisotropy highlights the importance of accounting for the orientation-dependent behavior of WAAM-fabricated components when designing parts for specific mechanical performance requirements.
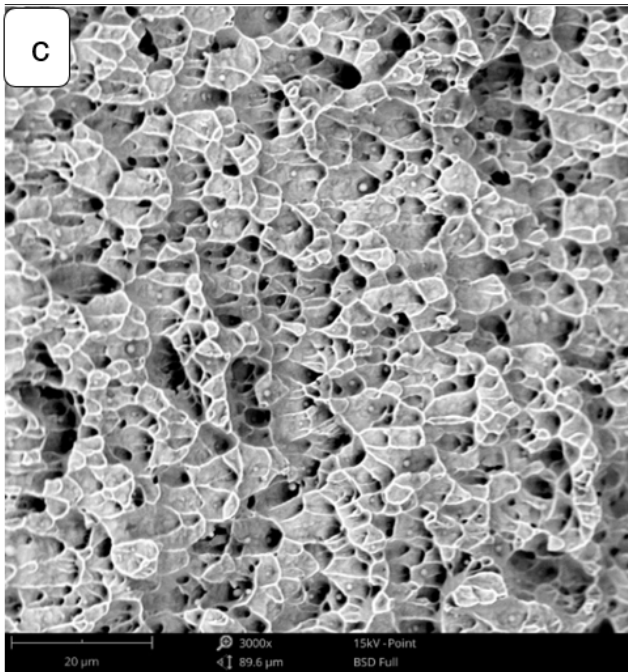
Theylor A. Amaya-Villabón, Andres F. Gil-Plazas, Oscar F. Mayorga-Rodríguez, Cristian R. Peña-Velandia, Julián D. Rubiano-Buitrago, David A. Ramírez-Vargas, Liz K. Herrera-Quintero

Figure 18. SEM images of tensile specimen fracture surfaces at different orientations: a) 0°, b) 45°, and c) 90°
Source: Authors

Several studies have reported similar ductile fracture characteristics in WAAM-fabricated stainless steels. For instance, [37] observed ductile fracture modes in WAAM-built 316L components, where dimples formed due to microvoid coalescence, reinforcing the presence of strong intergranular bonding. Similarly, [38] reported an anisotropic tensile behavior in WAAM stainless steels, highlighting the impact of columnar grain growth on fracture propagation. Moreover, [39] investigated the effect of processing parameters on the mechanical properties of WAAM-fabricated austenitic stainless steel and confirmed that directional solidification influences crack propagation. This aligns with our observations.

To optimize mechanical properties and reduce anisotropy, it is crucial to consider post-process treatments. Future work should explore the necessity of thermal treatments to refine the isotropy of mechanical properties. Such evaluations are essential for tailoring WAAM components to meet stringent performance criteria in industrial applications.

Conclusions

This study shows that the stability of the WAAM process is highly sensitive to the combination of voltage, WFS, and TS. Higher voltages necessitate higher WFS to maintain arc stability and minimize defects, while excessive TS (>300 mm/min) lead to surface irregularities (humps and valleys) that cannot be rectified in subsequent passes.

The bead dimensions (height and width) can be controlled by adjusting the voltage, WFS, and TS. Increasing the voltage and WFS results in broader but less tall deposits, whereas reducing TS and ensuring an adequate material feed promotes more uniform and stable bead geometry.

Low WFS levels correlate with higher porosity and inclusions, underscoring that parameter selection is critical for reducing internal defects. Ensuring optimal arc stability significantly enhances microstructural integrity and reduces the discontinuities within the deposited material.

Across all tested conditions, the 308L stainless steel deposits exhibited a typical microstructure, comprising γ-austenite and δ-ferrite phases, in line with literature reports. Variations in the heat input influenced the morphology of δ-ferrite, ranging from columnar and lathy to vermicular forms, underscoring the potential of thermal and process parameter control to refine the microstructure.

Although the yield strength remained unaffected by specimen orientation, UTS and elongation showed clear anisotropy. A 90° orientation yielded higher UTS values, and the 45° orientation entailed greater ductility. These anisotropic behaviors can be attributed to the directional grain growth and interlayer bonding conditions inherent to the WAAM process.

A fractographic analysis revealed ductile fracture with microvoid coalescence in all orientations. At 90°, the fractures followed the direction of the dendritic grain growth, confirming that the anisotropic microstructure directly influences fracture patterns and the mechanical response.

Acknowledgements

CRediT author statement

Andrés Fernando Gil Plazas and Theylor Andrés Amaya Villabón conceptualized the study, performed data curation and investigation, and were in charge of visualization. Theylor Andrés Amaya Villabón was entrusted with the communication and integration of the CNC router to the welding machine. Óscar Fabián Mayorga Rodríguez, Cristian Raúl Peña, and Julián David Rubiano Buitrago developed the methodology and conducted the formal analysis. David Alberto Ramírez, Liz Karen Herrera, and Andrés Fernando Gil Plazas were in charge of project administration and supervision, implemented the necessary software, and provided essential resources. Andrés Fernando Gil Plazas and Theylor Andrés Amaya Villabón led the writing of the original draft, to which all authors contributed. They were also in charge of reviewing and editing this manuscript.

Conflicts of interest

The authors declare no conflict of interest.

References

[1] L. Zhou *et al.*, "Additive manufacturing: A comprehensive review," *Sensors*, vol. 24, no. 9, art. 2668, 2024. https://doi.org/10.3390/s24092668

[2] A. Shah, R. Aliyev, H. Zeidler, and S. Krinke, "A review of the recent developments and challenges in wire arc additive manufacturing (WAAM) process," *J. Manuf. Mater. Process.*, vol. 7, no. 3, art. 97, 2023. https://doi.org/10.3390/jmmp7030097

[3] S. Ford and M. Despeisse, "Additive manufacturing and sustainability: An exploratory study of the advantages and challenges," *J. Clean. Prod.*, vol. 137, pp. 1573–1587, 2016. https://doi.org/10.1016/j.jclepro.2016.04.150

[4] *Additive manufacturing—General principles—Fundamentals and vocabulary*, ISO/ASTM 52900:2021, International Organization for Standardization, Geneva, Switzerland, 2021.

[5] G. Piscopo, E. Atzeni, A. Saboori, and A. Salmi, "An overview of the process mechanisms in the laser powder directed energy deposition," *Appl. Sci.*, vol. 13, no. 1, art. 117, 2023. https://doi.org/10.3390/app13010117

[6] M. M. Imran, A. C. Idris, L. C. De Silva, Y.-B. Kim, and P. E. Abas, "Advancements in 3D printing: Directed energy deposition techniques, defect analysis, and quality monitoring," *Technologies*, vol. 12, no. 6, art. 86, 2024. https://doi.org/10.3390/technologies12060086

[7] M. K. Thompson *et al.*, "Design for additive manufacturing: Trends, opportunities, considerations, and constraints," *CIRP Ann. Manuf. Technol.*, vol. 65, no. 2, pp. 737–760, 2016. https://doi.org/10.1016/j.cirp.2016.05.004

[8] S. W. Williams, F. Martina, A. C. Addison, J. Ding, G. Pardal, and P. Colegrove, "Wire + arc additive manufacturing," *Mater. Sci. Technol.*, vol. 32, no. 7, pp. 641–647, 2016. https://doi.org/10.1179/1743284715Y.0000000073

[9] J. D. Rubiano-Buitrago, A. F. Gil-Plazas, L. A. Boyacá-Mendivelso, and L. K. Herrera-Quintero, "Fused filament fabrication of WC-10Co hardmetals: A study on binder formulations and printing variables," *J. Manuf. Mater. Process.*, vol. 8, no. 3, art. 118, 2024. https://doi.org/10.3390/jmmp8030118

[10] A.-F. Gil-Plazas, J.-D. Rubiano-Buitrago, L.-A. Boyacá-Mendivelso, and L.-K. Herrera-Quintero, "Solid-state and super solidus liquid phase sintering of 4340 steel SLM powders shaped by fused filament fabrication," *Rev. Fac. Ing.*, vol. 31, no. 60, art. e13913, 2022. https://doi.org/10.19053/01211129.v31.n60.2022.13913

[11] K. S. Derekar, "A review of wire arc additive manufacturing and advances in wire arc additive manufacturing of aluminium," *Mater. Sci. Technol.*, vol. 34, no. 8, pp. 895–916, 2018. https://doi.org/10.1080/02670836.2018.1455012

[12] D. Ding, Z. Pan, D. Cuiuri, and H. Li, "Wire-feed additive manufacturing of metal components: Technologies, developments and future interests," *Int. J. Adv. Manuf. Technol.*, vol. 81, nos. 1–4, pp. 465–481, 2015. https://doi.org/10.1007/s00170-015-7077-3

[13] M. Abuabiah *et al.*, "Advancements in laser wire-feed metal additive manufacturing: A brief review," *Materials*, vol. 16, no. 5, art. 2030, 2023. https://doi.org/10.3390/ma16052030

[14] W. Jin *et al.*, "Wire arc additive manufacturing of stainless steels: A review," *Appl. Sci.*, vol. 10, no. 5, art. 1563, 2020. https://doi.org/10.3390/app10051563

[15] F. R. Teixeira, F. M. Scotti, R. P. Reis, and A. Scotti, "Effect of the CMT advanced process combined with an active cooling technique on macro and microstructural aspects of aluminum WAAM," *Rapid Prototyp. J.*, vol. 27, no. 6, pp. 1206–1219, 2021. https://doi.org/10.1108/RPJ-11-2020-0285

[16] T. A. Rodrigues *et al.*, "Wire and arc additive manufacturing of HSLA steel: Effect of thermal cycles on microstructure and mechanical properties," *Addit. Manuf.*, vol. 27, pp. 440–450, 2019. https://doi.org/10.1016/j.addma.2019.03.029

[17] P. Kyvelou *et al.*, "Mechanical and microstructural testing of wire and arc additively manufactured sheet material," *Mater. Des.*, vol. 192, art. 108675, 2020. https://doi.org/10.1016/j.matdes.2020.108675

[18] B. P. Nagasai, S. Malarvizhi, and V. Balasubramanian, "Mechanical properties of wire arc additive manufactured carbon steel cylindrical component made by gas metal arc welding process," *J. Mech. Behav. Mater.*, vol. 30, no. 1, pp. 188–198, 2021. https://doi.org/10.1515/jmbm-2021-0019

[19] Y. Li, C. Su, and J. Zhu, "Comprehensive review of wire arc additive manufacturing: Hardware system, physical process, monitoring, property characterization, application and future prospects," *Results Eng.*, vol. 13, art. 100330, 2022. https://doi.org/10.1016/j.rineng.2021.100330

[20] F. R. Teixeira *et al.*, "A methodology for shielding-gas selection in wire arc additive manufacturing with stainless steel," *Materials*, vol. 17, no. 13, art. 3328, 2024. https://doi.org/10.3390/ma17133328

[21] L. Segovia-Guerrero *et al.*, "Influence of printing parameters on the morphological characteristics of plasma directed energy-deposited stainless steel," *J. Manuf. Mater. Process.*, vol. 8, no. 5, art. 233, 2024. https://doi.org/10.3390/jmmp8050233

[22] R. P. Ferreira, L. O. Vilarinho, and A. Scotti, "Development and implementation of a software for wire arc additive manufacturing preprocessing planning: Trajectory planning and machine code generation," *Weld. World*, vol. 66, no. 3, pp. 455–470, 2022. https://doi.org/10.1007/s40194-021-01233-w

[23] F. Michel, H. Lockett, J. Ding, F. Martina, G. Marinelli, and S. Williams, "A modular path planning solution for wire + arc additive manufacturing," *Robot. Comput.-Integr. Manuf.*, vol. 60, pp. 1–11, 2019. https://doi.org/10.1016/j.rcim.2019.05.009

[24] H. Nagamatsu, H. Sasahara, Y. Mitsutake, and T. Hamamoto, "Development of a cooperative system for wire and arc additive manufacturing and machining," *Addit. Manuf.*, vol. 31, art. 100896, 2020. https://doi.org/10.1016/j.addma.2019.100896

[25] Y. Yehorov, L. J. da Silva, and A. Scotti, "Balancing WAAM production costs and wall surface quality through parameter selection: A case study of an Al-Mg5 alloy multi-layer non-oscillated single pass wall," *J. Manuf. Mater. Process.*, vol. 3, no. 2, art. 32, 2019. https://doi.org/10.3390/jmmp3020032

[26] B. Wu *et al.*, "A review of the wire arc additive manufacturing of metals: Properties, defects and quality improvement," *J. Manuf. Process.*, vol. 35, pp. 127–139, 2018. https://doi.org/10.1016/j.jmapro.2018.08.001

[27] L. Wang, J. Chen, C. Wu, and J. Gao, "Backward flowing molten metal in weld pool and its influence on humping bead in high-speed GMAW," *J. Mater. Process. Technol.*, vol. 237, pp. 342–350, 2016.

[28] X. Meng, G. Qin, and Z. Zou, "Investigation of humping defect in high-speed gas tungsten arc welding by numerical modelling," *Mater. Des.*, vol. 94, pp. 69–78, 2016. https://doi.org/10.1016/j.matdes.2016.01.019

[29] E. Kerber *et al.*, "Variable layer heights in wire arc additive manufacturing and WAAM information models," *Machines*, vol. 12, art. 432, 2024. https://doi.org/10.3390/machines12070432

[30] N. Solanke and R. M. Metkar, "Optimization of welding process parameters of wire arc additive manufacturing," *J. Phys. Conf. Ser.*, vol. 2763, art. 012018, 2024. https://doi.org/10.1088/1742-6596/2763/1/012018

[31] O. Panchenko *et al.*, "A high-performance WAAM process for Al–Mg–Mn using controlled short-circuiting metal transfer at increased wire feed rate and increased travel speed," *Mater. Des.*, vol. 195, art. 109040, 2020. https://doi.org/10.1016/j.matdes.2020.109040

[32] N. N. Dovzhenko *et al.*, "Structural element shaping on a plate in the manufacture of a hybrid product from aluminum alloy using WAAM technology," *Int. J. Adv. Manuf. Technol.*, vol. 123, pp. 3183–3204, 2022. https://doi.org/10.1007/s00170-022-10310-3

[33] S. Sharifi, M. Sadeghian, and P. Shamsaei, "Selection of parameters for optimized WAAM structures: Influence of deposition strategy and energy input," *Mater. Des.*, vol. 217, art. 110576, 2022. https://doi.org/10.3390/ma16134862

[34] S. Astafurov and E. Astafurova, "Phase composition of austenitic stainless steels in additive manufacturing: A review," *Metals*, vol. 11, no. 7, art. 1052, 2021. https://doi.org/10.3390/met11071052

[35] Y. Koli, S. Aravindan, and P. V. Rao, "Influence of heat input on the evolution of δ-ferrite grain morphology of SS308L fabricated using WAAM-CMT," *Mater. Charact.*, vol. 194, art. 112363, 2022. https://doi.org/10.1016/j.matchar.2022.112363

[36] J. A. Brooks, N. C. Y. Yang, and J. S. Krafcik, "Clarification on development of skeletal and lathy ferrite morphologies in stainless steel welds," *Sci. Technol. Weld. Join.*, vol. 6, no. 6, pp. 412–414, 2001. https://doi.org/10.1179/stw.2001.6.6.412

[37] J. Vora *et al.*, "Experimental investigations on mechanical properties of multi-layered structure fabricated by GMAW-based WAAM of SS316L," *J. Mater. Res. Technol.*, vol. 20, pp. 2748–2757, 2022. https://doi.org/10.1016/j.jmrt.2022.08.074

[38] P. Long *et al.*, "Microstructure evolution and mechanical properties of a wire-arc additive manufactured austenitic stainless steel: Effect of processing parameter," *Materials*, vol. 14, art. 1681, 2021. https://doi.org/10.3390/ma14071681

[39] N. Duraisamy, R. L. Nayak, A. Gokhale, and S. K. Sinha, "Tensile behavior of wire arc additive manufactured stainless steel structure: Microstructure and fracture analysis," *J. Mater. Process. Technol.*, vol. 268, pp. 177–190, 2019.